Weak Gravitational Lensing by the Nearby Cluster Abell 3667

Michael Joffre[1,2,7], Philippe Fischer[3,7], Joshua Frieman[1,2,7], Timothy McKay[4,7], Joseph J. Mohr[1,6,7], Robert C. Nichol[5,7], David Johnston[1,2], Erin Sheldon[4] and Gary Bernstein[3]

ABSTRACT

We present two weak lensing reconstructions of the nearby ($z_{cl} = 0.055$) merging cluster Abell 3667, based on observations taken ~ 1 year apart under different seeing conditions. This is the lowest redshift cluster with a weak lensing mass reconstruction to date. The reproducibility of features in the two mass maps demonstrate that weak lensing studies of low-redshift clusters are feasible. These data constitute the first results from an X-ray luminosity-selected weak lensing survey of 19 low-redshift ($z < 0.1$) southern clusters.

Subject headings: galaxies: clusters: individual (Abell 3667), gravitational lensing

1. Introduction

Weak gravitational lensing—measurement of the induced shear of distant galaxy images to infer the foreground mass distribution—has now become a standard tool to probe dark matter in galaxy clusters. Since the work of Tyson et al. (1990), weak lensing studies of over twenty galaxy clusters have been published (Mellier 1999). In all cases to date, the observations have been confined to moderate to high-redshift clusters, $z_{cl} > 0.15$*, for two reasons: (i) the cluster lensing strength is maximized if the angular diameter distance to the foreground cluster is roughly half that of the background source galaxies, which at a limiting depth of $R \sim 25$ are typically at $\langle z_s \rangle \sim 1$; (ii) a distant cluster subtends an area on the sky which can be roughly encompassed by a single CCD chip, allowing deep exposures of the entire field in moderate observing time. Unfortunately, most of our knowledge of cluster properties comes from X-ray and dynamical (optical redshift) studies, which are much more easily conducted for nearby clusters. This mismatch between the observing requirements for weak lensing and dynamical studies has hampered direct comparison of these mass measuring techniques. It would be beneficial to have weak lensing observations for a sample of nearby clusters. This would enable more detailed studies of the cluster binding mass, baryon fraction, and morphology.

For weak lensing studies, nearby clusters have the advantage that their background galaxies are relatively well resolved (reducing the effect of PSF smearing) and their inferred projected mass distributions are relatively insensitive to the uncertain background source galaxy redshift distribution in the limit $z_{cl} \ll z_s$. The advent of CCD mosaic cameras on 4m telescopes, coupled with developments in weak lensing analysis, now make possible wide-field studies of weak lensing in nearby clusters (Joffre et al. 1999; Stebbins et al. 1996).

With these benefits in mind, we have begun

[1]Dept. of Astronomy and Astrophysics, University of Chicago, Chicago IL
Email:joffre@coltrane.uchicago.edu

[2]NASA/Fermilab Astrophysics Center, Fermi National Accelerator Lab, Batavia, IL

[3]Dept. of Astronomy, University of Michigan, Ann Arbor, MI

[4]Dept. of Physics, University of Michigan, Ann Arbor, MI

[5]Physics Department, Carnegie Mellon University, Pittsburgh, PA

[6]Chandra Fellow

[7]Visiting Astronomer, National Optical Astronomy Observatories, which is operated by the Association of Universities for Research in Astronomy, Inc., under contract to the National Science Foundation

*Lensed arcs have been detected in two low-redshift clusters (Blakeslee & Metzger 1998; Campusano et al. 1998), but such instances of strong lensing only probe the cores of clusters.

a complete, X-ray luminosity-selected weak lensing survey of 19 nearby ($z_{cl} < 0.1$) Southern clusters (Joffre et al. 1999); this sample, drawn from the XBACS (Ebeling et al. 1996), is also being targeted by the Viper telescope for Sunyaev-Zel'dovich observations (Romer et al. 1999). As of October 1999, we have completed imaging observations of 9 clusters in the sample, using the BTC and Mosaic II cameras at the 4m telescope at CTIO. In this Letter, we present results for our first target, the $z = 0.055$ cluster Abell 3667.

The major obstacle to weak lensing studies of nearby clusters is the small shear signal they produce. Shear estimates are limited by the intrinsic ellipticity of the background galaxies (shape noise) and PSF anisotropies. To create reliable mass maps we must therefore measure ellipticities for a large number of background galaxies and correct for the PSF anisotropy very accurately. Given that we expect cluster-induced shears of at most $\sim 5\%$, we have reduced systematic sources of shear, which include atmospheric turbulence, telescope shake, and optical aberration, to less than 0.5% across the images (based on the corrected stellar ellipticities). As proof of our ability to make these measurements, we present weak lensing analyses of A3667 based on two sets of observations taken ~ 1 year apart under different seeing conditions and with different observing strategies.

2. Observations

Much ancillary information is available for Abell 3667. Based on redshifts for 154 cluster members (Sodre et al. 1992; Katgert et al. 1996), an optical velocity dispersion in the range $\sigma_v = 970-1200$ km/s has been inferred (Sodre et al. 1992; Fadda et al. 1996). From the ROSAT All-Sky Survey, the X-ray luminosity $L_X = 6.5 \times 10^{44}$ ergs/s (Ebeling et al. 1996), among the strongest X-ray sources in the southern sky. The radio map shows a double halo structure (Rottgering et al. 1997). The A3667 field contains two dominant D galaxies; the ROSAT PSPC image (Knopp et al. 1996) and ASCA temperature map (Markevitch et al. 1998) indicate the cluster is undergoing a merger along the direction (Knopp et al. 1996) joining them.

We observed A3667 on two separate runs with the BTC (Wittman et al. 1998) at the CTIO 4m telescope. The BTC is a 4096×4096 pixel camera with a pixel scale of $0.43''$; there are significant gaps between the four chips that must be removed from the final combined image by dithering exposures. In June 1997, two of us (PF and JM) observed A3667 in the R and B_J bands in relatively poor seeing (combined stellar FWHM of $1.55'' \pm 0.15''$ in R). The combined image in each filter covers an approximate area $42' \times 42'$, with a maximum surface brightness limit of 28.6 mag arcsec^{-2} in R and 28.9 mag arcsec^{-2} in B_J, corresponding to 1σ in the sky. Total observing times were 5500s in B_J and 15500s in R. We denote these the 'α' set of images in our analysis. In September 1998, three of us (JF, TM, RN) observed A3667 under better seeing conditions (combined stellar FWHM $= 1.23'' \pm 0.07''$ in R), covering a $44' \times 44'$ area to a maximum surface brightness limit of 28.2 mag arcsec^{-2} in R and 27.9 mag arcsec^{-2} in B. This corresponded to a total observing time of 12600s in R and 2250s in B. We also obtained I-band images which we have used to construct a color-magnitude diagram to remove cluster members from the background sample. (Due to fringing effects, the I-band data was not used in the lensing analysis itself.) We denote these better-seeing images the 'β' set.

After debiasing and flatfielding of the frames, the frames were coadded. BTC observations of USNO astrometric fields were used to remove field distortion from the images. Objects were detected using SExtractor (v2.1.0) (Bertin & Arnouts 1996). Our own code measures quadrupole moments Q_{ij} of each object using the adaptive Gaussian weighting scheme of Bernstein, et al.(2000): the image is multiplied by an elliptical Gaussian weight function, the shape of which is successively iterated to match the object's ellipticity. This routine returns estimates of the ellipticity vectors $e_1 = (Q_{11} - Q_{22})/(Q_{11} + Q_{22})$ and $e_2 = 2Q_{12}/(Q_{11} + Q_{22})$ and their uncertainties. The unsaturated bright stars in each image were used to characterize the PSF anisotropy as a function of position. Following Fischer & Tyson (1997), we convolved the images with a spatially varying kernel which circularizes the stellar images. We then repeat the detection and measurement of background galaxies in the PSF-corrected images. The moments of each galaxy are finally corrected for isotropic PSF

dilution using the simulations and analytic results of Bernstein, et al.(2000); the correction factor depends upon galaxy image size relative to the PSF and upon the image profile. Objects in the background galaxy samples for the lensing analysis are selected to have magnitudes $R < 24.75$, $B < 24.5$, and $B_J < 25.5$. They are also required to have half-light radii at least 1.5 times that of the PSF. The $R - I$ color-magnitude diagram is used to remove red cluster members from the background sample brighter than $R = 22$. These cuts ensure that the object moments can be accurately measured ($S/N > 8 - 10\sigma$), that stellar contamination is minimal, and that the vast majority of the sample lies well behind the cluster. The resulting samples contain approximately 11,000 background galaxies for the α R image, 30,000 for the β R, 18,000 for the α B_J, and 11,000 objects for the β B image. We note that the β R image has a larger number of galaxies than the α set, although the later has a longer exposure time. This is due to the fact that the β images covered a larger area on the sky and the poor seeing of the α R image makes galaxies and stars difficult to distinguish. Many of these smaller galaxies are lost when we cut on half-light radius.

3. Comparison

To study the robustness of the mass maps derived from the two sets of observations, we first examine the consistency of the measured ellipticities of background galaxies. We focus on the shear measurements (as opposed to the mass maps themselves) because we expect the errors to be uncorrelated in different regions of the sky. In principle, differences in seeing, imaging depth, and filters will lead to differences between the shear fields estimated from the two observations. However, after applying the corrections discussed above, the derived shear fields should be strongly correlated.

We trimmed the R and B band images in the α and β datasets to the regions common to both and calculated the mean ellipticities of the background galaxies in 100 angular bins of width $\sim 25''$. To quantify the consistency of the two fields we calculate the χ^2 value for the ellipticities for each filter,

$$\chi^2 = \sum_{i=1}^{2} \sum_{N_b=1}^{100} \frac{(e_{i\alpha} - e_{i\beta})^2}{(\sigma^2_{e_{i\alpha}} + \sigma^2_{e_{i\beta}})} \ .$$

The estimate of the ellipticity variance in a spatial bin for a given data set is

$$\sigma^2_{ei} = (N_c/N^2)\langle\sigma^2_m\rangle_c + (N_d/N)^2\sigma^2_{rms}/(N_d - 1),$$

where N is the total number of background galaxies in the bin and N_c and N_d are the numbers of galaxies in the bin with and without counterparts in the other data set. $\langle\sigma^2_m\rangle_c$ is the average measurement error in e_i derived from our measurement uncertainties in Q_{ij} for the galaxies common to both sets; σ_{rms} is the *rms* spread in the ellipticities of the N_d galaxies in the bin not found in the other set. That is, for galaxies measured in both data sets, we use the measurement uncertainty rather than the rms per bin to take into account the correlation between the data sets.

Figure 1a shows the binned ellipticities of background galaxies found in both data sets in the R band; the reduced χ^2 is 1.11 for 200 d.o.f. Fig. 1b compares the ellipticities for all galaxies: in this case, the scatter between the datasets is significantly larger, as expected since they are no longer confined to the same galaxies; the reduced χ^2 for all the objects is 1.19, implying a probability $P(\chi^2|200) = 3.5\%$ in the case of random errors. The average ellipticity in Fig. 1b is $2.57 \pm 0.22\%$ for the α set and $2.42 \pm 0.16\%$ for the β set. As expected for low redshift cluster lensing, the maximum tangential ellipticity is only 4%, while the majority of the signal is $\sim 1\%$. The major contribution to χ^2 comes from a few bins located at the edge of the images; removing the two worst bins drops χ^2 substantially, raising the probability that the ellipticities are consistent within the errors to $\sim 30\%$. The edges of our images have the largest field distortions and shallowest coverage and are therefore where we expect the largest discrepancy between the data sets. For the blue filters, due to the shallowness of the β set and the fact that the B and B_J filters are not identical, there are very few background objects in common ($\sim$ 1000 vs. 9000 in the R images). The error in χ^2 is dominated by the rms ellipticity, giving a value of $\chi^2 = 1.125$ or $P(\chi^2|200) = 10.9\%$. This is a very strict test of our measurement and correction algorithm, showing that our shear

measurements are reproducible. The relatively low formal probabilities may be due to either small residual systematics or slight underestimates of the measurement error. Across the image, the high correlation between the corrected data sets is quite encouraging, with large differences generally confined to small areas near the edge of the field.

We performed mass reconstruction on a 60×60 grid, applying a version of the Kaiser and Squires (Squires et al. 1996) algorithm separately to the blue and red catalogs and combining them by weighting the mass at each gridpoint by its S/N. We have chosen to plot the S/N of each mass map pixel as this gives a direct picture of which mass peaks are significant. We estimated the the noise in each pixel for this map as follows: we rotated each galaxy orientation through an arbitrary angle and then computed the resulting mass map; we then repeated this procedure 100 times and estimated the noise from the variance of these 100 noise maps. As a check of systematics, we produced mass maps for each image with all galaxy orientations rotated by 45 degrees and found no significant features. In the absence of residual systematic effects such a map should be consistent with noise (Stebbins et al. 1996; Kaiser et al. 1994). As an additional systematics check, we have made shear maps for the stars in each filter; they are consistent with noise, as expected.

The combined convergence maps are shown in Figures 2 and 3 for the α and β data sets. There is remarkable agreement in morphology of the two maps, and the largest mass features appear to be robust. To quantify this correlation, we calculate Pearson's r between the two mass maps:

$$r = \frac{\sum^N (m_\alpha - \langle m_\alpha \rangle)(m_\beta - \langle m_\beta \rangle)}{\sqrt{\sum^N (m_\alpha - \langle m_\alpha \rangle)^2} \sqrt{\sum^N (m_\beta - \langle m_\beta \rangle)^2}},$$

where m is the value of a mass map pixel and N is the total number of gridpoints. $r = -1$ for completely anticorrelated data, 0 for uncorrelated data, and 1 for completely correlated data. We find a value of $r = 0.6$ between the two maps, indicating that they are in fact correlated. The formal probability of achieving such a high value of r by chance for uncorrelated maps is $\mathrm{erfc}(|\mathrm{r}|\sqrt{\mathrm{N}/2})$, negligibly small for 3600 gridpoints. To further quantify the degree of correlation, we calculated Pearson's r between the 100 noise maps described above and found these maps gave a value of -0.009 ± 0.089. To determine the correlations between the entire maps, rather than the correlation introduced by the coincidence of the central peak, we masked out a box centered on the two maps with a size of $10'$. When Pearson's r was computed on the remaining unmasked areas, we still found a value of $r = 0.40$. This value remained fairly constant as we increased the masked region until the masked region's size approached that of the two images. Inspection of the maps indicates that even the relatively low significance ($\sim 3\sigma$) mass peaks which correspond to a convergence of ~ 0.02 are reproducible. We quantified this by masking regions greater than 3σ in either map and computing Pearson's r on the unmasked portions. The value of the correlation only dropped to $r = 0.27$. We note that r dropped quickly to zero if we masked out all regions of significance lower than 3σ. We have also implemented the mass reconstruction algorithm of Seitz & Schneider (1998) and find the same correlation between features.

The mass map is strongly peaked around the central D galaxy and generally correlates well with both the cluster light and ROSAT X-ray flux distributions (Joffre et al. 2000). At lower significance, there also appears to be mass associated with the second bright D galaxy in the NW of the image and with cluster galaxies in the N and SE of the central D.

4. Conclusion

We have detected weak lensing at the $0.5 - 4\%$ level in a nearby galaxy cluster using two separate sets of images. Despite differences in depth, seeing, and filters, the shear maps are consistent within the errors, and the reconstructed mass maps are strongly correlated. This reproducibility demonstrates the feasibility of using weak lensing to probe the mass distribution in low-redshift clusters. In future work, we will apply these methods to all the clusters in our survey and compare the resulting mass maps with X-ray, optical, and Sunyaev-Zel'dovich data to obtain a more detailed picture of the properties of nearby clusters.

This work is supported in part by Chandra Fellowship grant PF8-1003, awarded through the Chandra Science Center. The Chandra Science Center is operated by the Smithsonian Astrophysical Observatory for NASA under contract NAS8-39073. This research was supported in part by the DOE and by NASA grant NAG5-7092 at Fermilab and NSF PECASE grant AST 9703282 at the University of Michigan.

REFERENCES

Bernstein, G., et al, 2000 in preparation

Bertin, E. & Arnouts, S. 1996, AA, 117,393

Blakeslee, J. P. & Metzger, M. R. 1999, ApJ, 513, 592

Campusano, L. D., Kneib, J. P., & Hardy, E. 1998, ApJ, 496, L79

Ebeling, H., et al. 1996, MNRAS, 281, 799.

Fadda, D., et al. 1996, ApJ, 473,670

Fischer, P. & Tyson, J. A. 1997, AJ, 114, 14

Joffre, M., et al. 1999, to appear in "Gravitational Lensing: Recent progress and Future Goals," ed. T.Brainerd and C.Kochanek, ASP Conf Series, astro-ph/9909029

Joffre, M., et al. 2000 in preparation

Kaiser, N., et al. 1994, astro-ph/9407004.

Katgert, P. et al. 1996, AA, 310, 8

Knopp,G., et al. 1996, ApJ, 472, 125

Markevitch, M., Sarazin, C. L., & Vikhlinin, A. 1998, ApJ, 521, 526

Mellier, Y. 1999, astro-ph/9812172, ARAA, to appear

Romer, A. K., Griffin, G., Peterson, J. B., Nichol, R. C., Newcomb, M. 1999, BAAS 31, 3, 58.03.

Rottgering, H.J.A., et al. 1997,MNRAS, 290,577

Seitz, S. & Schneider, P. astroph/9802051

Sodre, L., Capelato, H. V., Steiner, J. E., Proust, D., & Mazure, A. 1992, MNRAS, 259, 233

Squires, G., et al. 1996, ApJ, 461,572

Stebbins, A., et al. 1996, Proceedings of the IAU Symposium 173, 75

Tyson, J. A., Wenk, R. A., & Valdes, F. 1990, ApJ, 349, L1

Wittman, D., et al. 1998, Proc. SPIE, 3355, 626

This 2-column preprint was prepared with the AAS LaTeX macros v5.0.

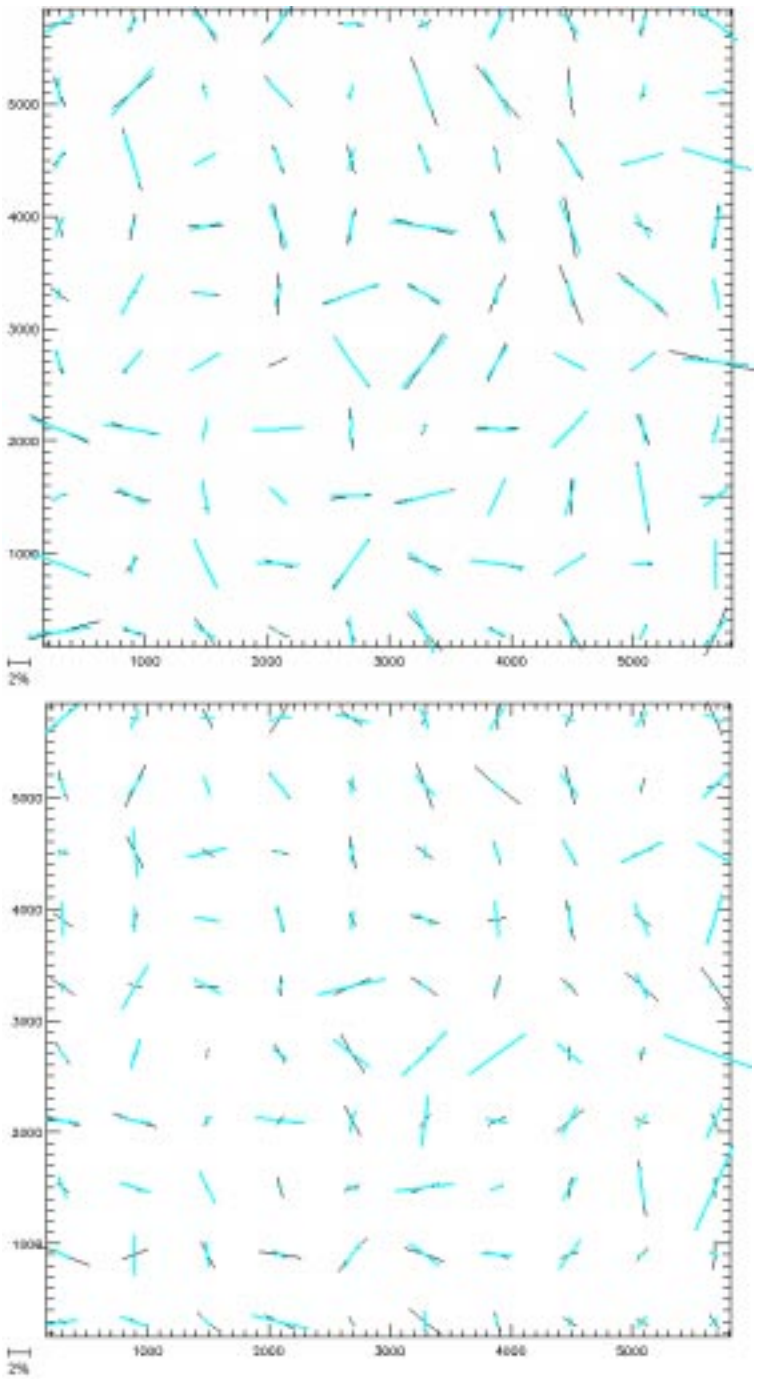

Fig. 1.— (a) The binned average ellipticities of background galaxies appearing in both R band images, light blue for the α data set and black for the β data set. (b) The same for all background galaxies. The units are CCD pixels; an ellipticity of 2% is shown in the lower left.

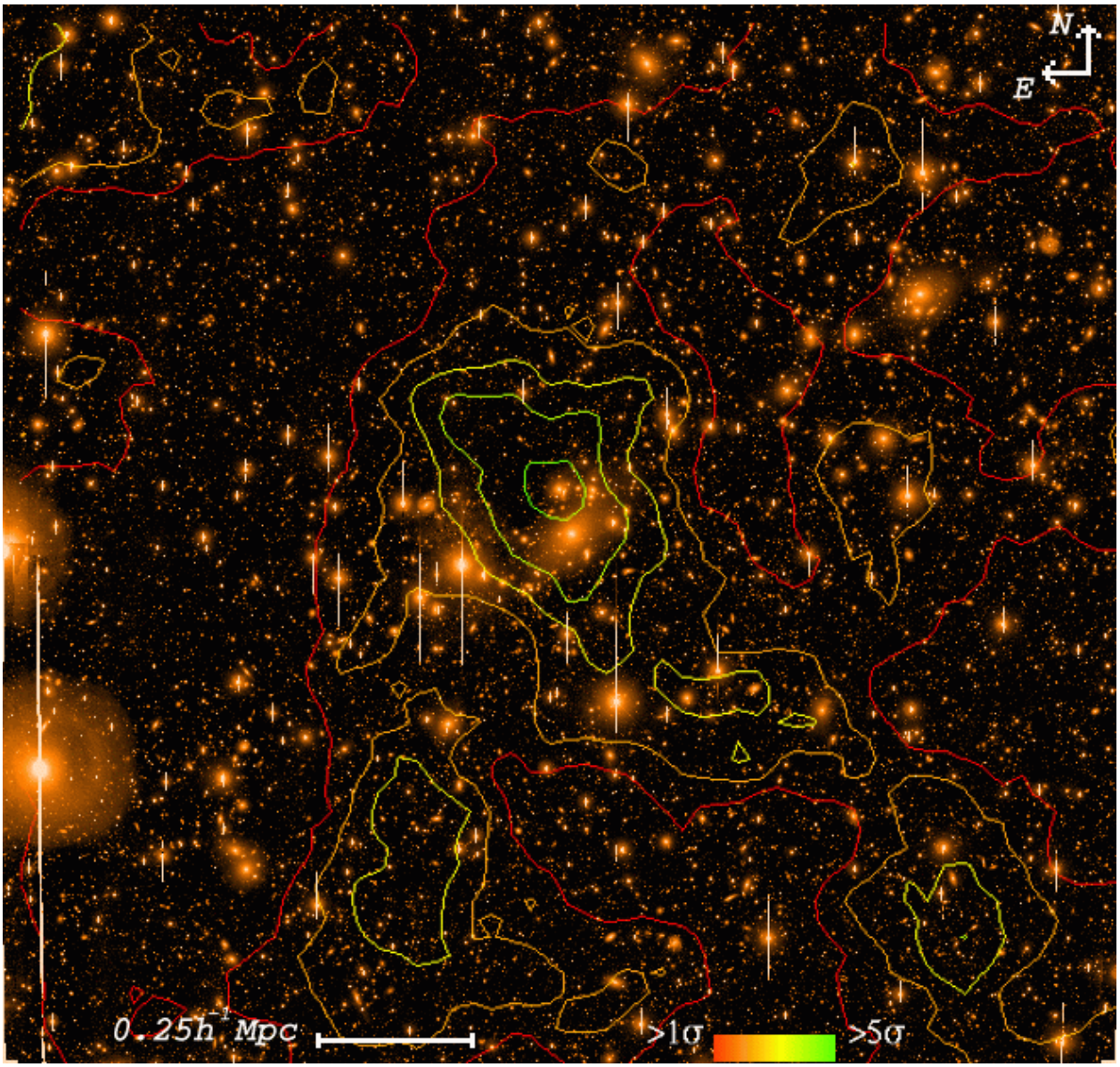

Fig. 2.— Projected mass map of A3667 for set α. Contours correspond to a change in signal to noise of unity; only contours $\geq 1\sigma$ are shown. The mass map is superimposed upon the α R image. The image is $42' \times 42'$.

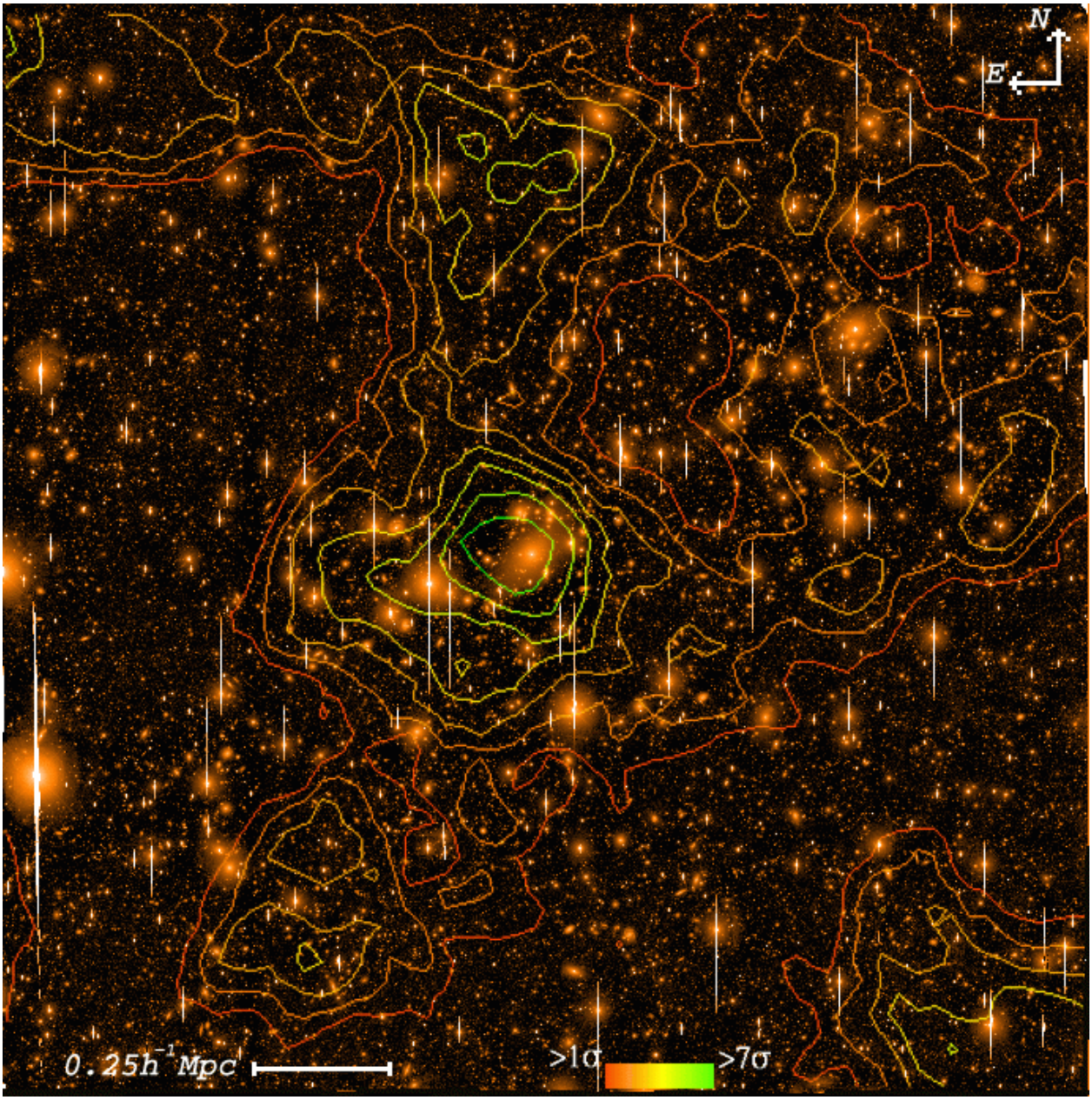

Fig. 3.— Projected mass map of A3667 for set β. The mass map is superimposed upon the β R image. The image is $44' \times 44'$.